



## Recurrence quantification analysis of rs-fMRI data: A method to detect subtle changes in the TgF344-AD rat model



Arash Rezaei<sup>a</sup>, Monica van den Berg<sup>b,c</sup>, Hajar Mirlohi<sup>a</sup>, Marleen Verhoye<sup>b,c</sup>, Mahmood Amiri<sup>d,\*</sup>, Georgios A. Keliris<sup>b,c,e</sup>

<sup>a</sup> Medical Biology Research Center, Institute of Health Technology, Kermanshah University of Medical Sciences, Kermanshah, Iran

<sup>b</sup> Bio-Imaging Lab, University of Antwerp, Belgium

<sup>c</sup> iNEURO Research Centre of Excellence, University of Antwerp, Antwerp, Belgium

<sup>d</sup> Medical Technology Research Center, Institute of Health Technology, Kermanshah University of Medical Sciences, Kermanshah, Iran

<sup>e</sup> Institute of Computer Science, Foundation for Research & Technology, Hellas, Heraklion, Crete, Greece

### ARTICLE INFO

#### Keywords:

Alzheimer's disease  
Recurrence quantification analysis  
fMRI  
Functional connectivity

### ABSTRACT

**Background and objective:** Alzheimer's disease (AD) is one of the leading causes of dementia, affecting the world's population at a growing rate. The preclinical stage of AD lasts over a decade, hence understanding AD-related early neuropathological effects on brain function at this stage facilitates early detection of the disease.

**Methods:** Resting-state functional magnetic resonance imaging (rs-fMRI) has been a powerful tool for understanding brain function, and it has been widely used in AD research. In this study, we apply Recurrence Quantification Analysis (RQA) on rs-fMRI images of 4-months (4 m) and 6-months-old (6 m) TgF344-AD rats and WT littermates to identify changes related to the AD phenotype and aging. RQA has been focused on areas of the default mode-like network (DMLN) and was performed based on Recurrence Plots (RP). RP is a mathematical representation of any dynamical system that evolves over time as a set of its state recurrences. In this paper, RPs were extracted in order to identify the affected regions of the DMLN at very early stages of AD.

**Results:** Using the RQA approach, we identified significant changes related to the AD phenotype at 4 m and/or 6 m in several areas of the rat DMLN including the BFB, Hippocampal fields CA1 and CA3, CG1, CG2, PrL, PtA, RSC, TeA, V1, V2. In addition, with age, brain activity of WT rats showed less predictability, while the AD rats presented reduced decline of predictability.

**Conclusions:** The results of this study demonstrate that RQA of rs-fMRI data is a potent approach that can detect subtle changes which might be missed by other methodologies due to the brain's non-linear dynamics. Moreover, this study provides helpful information about specific areas involved in AD pathology at very early stages of the disease in a very promising rat model of AD. Our results provide valuable information for the development of early detection methods and novel diagnosis tools for AD.

### 1. Introduction

Alzheimer's disease (AD) is a neurodegenerative disorder that leads to a progressive loss in memory and other cognitive functions. There is no specific treatment for this brain abnormality and in the long run, the affected individual will be unable to perform basic daily activities. The number of people worldwide suffering from AD is increasing and is expected to rise to 150 million by 2050 [1]. Moreover, the social and economic influences caused by AD impose increasing pressure on the healthcare systems worldwide. Hence, precise diagnosis and most

importantly early AD detection are thought to be crucial for improving the chances of potential treatments.

In humans, AD is believed to start at least 20 years before any apparent symptoms emerge. The hallmark pathologies of AD include i) the clustering of amyloid-beta segments in the extracellular space, forming what is known as amyloid plaques, and ii) irregular accumulations of tau protein inside neurons forming neurofibrillary tangles (NFT). The deposition of these proteins leads to variations in the brain which do not initially result in noticeable symptoms to the patient, but include gradual synaptic and neuronal loss [2,3]. After years of brain

\* Corresponding author.

E-mail address: [Ma\\_amiri\\_bme@yahoo.com](mailto:Ma_amiri_bme@yahoo.com) (M. Amiri).

alterations, some noticeable symptoms appear, such as memory loss and language issues [4]. However, studies show that instead of the presence of plaques or NFT, the symptomatic onset of AD is most significantly correlated with other parameters such as synaptic loss [5–8]. On these grounds, it is evident that at the early stages of AD, certain subtle changes in the brain such as alterations in connectivity might occur before the onset of symptoms but could potentially be detectable with imaging techniques such as magnetic resonance imaging (MRI).

Resting state functional MRI (rs-fMRI) gives substantial and non-invasive insights into brain functionality at rest and has been demonstrated to be a robust tool for studying the effects of synaptic dysfunction caused by advanced AD [9]. During rs-fMRI, spontaneous brain activity induces changes to the blood oxygenation level-dependent (BOLD) signal that indirectly relates to neural activity as a result of neurovascular coupling [10]. Typical rs-fMRI analysis techniques investigate functional connectivity (FC), which is defined as the correlation between BOLD time courses in two regions of interest over time, calculated by Pearson's correlation coefficient. Even though this standard analysis approach of rs-fMRI data yielded valuable insights into changes in brain connectivity, predicting in advance which person will develop AD at later stages in life from FC that is estimated based on correlations across the whole duration of a several minutes scan, remains challenging.

Recently, many studies have focused on the classification between healthy subjects and those at different stages of dementia such as AD, mild cognitive impairment (MCI), and early mild cognitive impairment (eMCI) using rs-fMRI images and machine learning with relatively good accuracies reaching over 80 % [11–18]. Kazemi et al. and Tajammal et al. used fMRI images of individuals from different stages of AD such as those with significant memory concern (SMC), eMCI, late-MCI (lMCI), and AD. By applying an alternative approach that used convolutional neural networks (CNN), they were able to achieve accuracies over 90 % demonstrating that the specific data analysis method employed can provide improvement in classification [19,20]. While these studies found overwhelmingly positive results in AD and eMCI diagnosis, the neural damage and loss of connections in the brain start prior to eMCI. Due to the insufficient size of datasets and the difficulty of diagnosing AD at the presymptomatic stages, machine learning methods pose particular challenges. This is because most machine learning algorithms require a substantial amount of data to produce reliable diagnosis [21]. Hence, this indicates the pressing need for development of novel analysis approaches that would be more sensitive and able to perform better with less amount of data.

The brain can be considered a non-linear dynamic system in which information processing occurs in various regions and neural circuits [22]. Neurons in the brain, function in a non-linear step-like fashion and networks of brain regions can also behave non-linearly [23]. The rate of state transitions in the brain (i.e., neurodynamics) and the existence of noise in neuronal systems have been combined into the frame of stochastic dynamical systems theory [24]. The physiology and functioning of the brain suggest that the brain may be accurately modeled as a non-linear complex system. While linear approaches work to some extent and give some understanding of the system's characteristics, non-linear methods are more effective and sensitive, revealing further insights into the brain functionality [25].

Natural dynamics can exhibit both regular and sporadic behavior. In deterministic dynamical systems or non-linear systems, the recurrence of states, or states that become arbitrarily similar after a period, is discernible. A recurrence plot (RP), developed by Eckmann et al. [26], visualizes these recurrences. An RP represents the occurrences in phase space when a state recurs. RP reduces an m-dimensional phase space trajectory of a system to a two-dimensional representation of its recurrences [27]. The essential concepts of recurrence stem from the Poincaré's Recurrence theorem, which states that comparable circumstances typically develop similarly, and that certain scenarios occur several times [25,28].

Dynamical systems theory has been used in fMRI studies [24]. From

this point of view, the fMRI data is considered as the characterization of a non-linear dynamic system evolving in time [25]. Here, we put forward the hypothesis that using a dynamical, non-linear approach for analyzing rs-fMRI data and classifying progression of AD at different stages can be advantageous. Specifically, we conjectured that using the concept of recurrence as represented in RPs, can characterize the system's behavior in the phase space, and the quantification of RPs provides a mathematically objective approach for evaluating the dynamical system [27]. More specifically, Recurrence Quantification Analysis (RQA) computes non-linear metrics from recurrence plots. RP and RQA have found extensive applications in the economy [29,30], physiology [31,32], neuroscience [33–35], and engineering [36,37]. Former studies revealed disturbed FC in Parkinson's diseases and hyperconnectivity caused by lupus using RPs [38,39], demonstrating the possibility of applying RP to fMRI data, to investigate altered brain function due to neurological disorders.

Given the non-linearity of brain function recorded by rs-fMRI, RQA can potentially capture intrinsic patterns of neural activity more effectively compared to other linear approaches. Most methods such as FC have lower temporal resolution than RP as the signals are either averaged first or a sliding window is moved alongside them to segment the original time-series [40–42]. This can lead to missing short- and long-lived spatio-temporal patterns in neural activity. While other methods with higher temporal resolution have been proposed, such as quasi-periodic pattern analysis (QPP) [43,44], in the current context, RP extracts a 5-dimensional model of the fMRI signals with 3 spatial dimensions and 2 temporal dimensions (A single RP is a 2 dimensional image with both dimensions representing time; in the case of fMRI images, a RP is calculated for each voxel the coordinates of which corresponds to 3 spatial dimensions). This significant emphasis on functionality through time coupled with the inherently non-linear nature of the method, renders RP and subsequently RQA a robust tool to detect short or long spatio-temporal patterns in the brain. Furthermore, considering that early stages of AD manifest with subtle synaptic changes, linear and low dimensional methods might overlook crucial biomarkers that can lead to early detection and further insights into the disease.

The contributions of this study are twofold. First, we demonstrate the application of the RQA method on rs-fMRI images to gain knowledge into early-stage AD and its effects on brain function; second, by doing so we show the abilities of RQA in discovering patterns of neural activity. To test our hypothesis, given that diagnostic tools which detect the early-presymptomatic stages of AD in humans are not available, in this study we employed the use of a very promising animal model of AD, specifically the TgF344-AD rat model. The rats of this model express human APP<sub>swe</sub> and PS1<sub>ΔE9</sub> mutations, and demonstrate all the major hallmarks of AD such as amyloid plaques and accumulation of rat tau proteins from 6 months onward [45,46], that in turn cause neuronal degeneration and cognitive impairment similar to that observed in humans [47]. To better understand the subtle changes happening at early-stages of AD, and demonstrate the utility of RP and RQA analysis, we used 4-, and 6-months old rats, resembling respectively the pre-plaque and early-plaque stage of AD in humans [48]. Our results revealed that both age as well as the AD phenotype induce changes in recurrent neural activity as reflected in RPs, and could help identifying the affected brain regions. Consequently, we concluded that RP and RQA demonstrate a huge potential to be utilized as future diagnostic tools for the early detection of brain activity alterations in AD.

## 2. Material

### 2.1. Animals

TgF344-AD rats (AD;  $N = 15$ ), and wild-type (WT;  $N = 11$ ) littermates underwent MRI at 4 and 6 months of age (datasets labeled as AD\_4m, WT\_4m, and AD\_6m, WT\_6m). Animals were housed in pairs in

an animal care facility with a 12 h light/dark cycle under controlled temperature (20–24 °C) and humidity (40–60 %). Rats had access to standard food and water ad libitum. All procedures were in accordance with the guidelines of the European Ethics Committee (decree 2010/63/EU). The research was approved by the Committee on Animal Care and Use at the University of Antwerp, Belgium (approval number: 2019-06).

## 2.2. rs-fMRI acquisition

Anesthesia was induced using isoflurane (5 % for induction and 2 % during handling procedures). The animals were endotracheally intubated and mechanically ventilated (70 breaths per minute) using a ventilator (Microventilator, Carfil, Belgium) with 2 % isoflurane. Anesthesia during the resting state fMRI scan consisted of an intravenous bolus injection of medetomidine (0.05 mg kg<sup>-1</sup>, Domitor®, Pfizer, Germany) and Pancuroniumbromide (0.5 mg kg<sup>-1</sup>, VWR, Belgium), followed by infusion of medetomidine (0.1 mg kg<sup>-1</sup>/hr) and Pancuroniumbromide (0.5 mg kg<sup>-1</sup>/hr), along with 0.4 % isoflurane. Body temperature was maintained at (37 ± 0.5) °C using a feedback-controlled warm air circuitry (MR-compatible Small Animal Heating System, SA Instruments, Inc., USA). Breathing rate, heart rate, and blood oxygenation were constantly monitored throughout the scan (MR-compatible Small Animal Monitoring and Gating System, SA Instruments, Inc., USA).

Data were acquired using a 9.4T Biospec MRI system (Bruker Bio-Spin, Germany) with Paravision 6 software application. After slice positioning, local shimming with an ellipsoid volume was performed to correct for magnetic field inhomogeneity within the volume of interest. Resting-state functional MRI (rs-fMRI) was acquired using a single-shot gradient-echo EPI-sequence with TR: 600 ms, TE: 18 ms, FOV: (30×30) mm<sup>2</sup>, imaging matrix: [96×96], number of coronal slices: 12, slice thickness: 1.0 mm, and a number of repetitions: 1000. In addition, T2-weighted 3D images were acquired using a 3D RARE sequence with TR: 2500 ms, TE: 44 ms, FOV: (30×30×22) mm<sup>3</sup>, imaging matrix: [256×256×128], and RARE-factor: 16. At the end of the scan, a subcutaneous injection of 0.1 mg kg<sup>-1</sup> atipamezole (Antisedan®, Pfizer, Germany) was administered to counteract the effects of the medetomidine anesthesia. Then, the animals were put on a second ventilator and heating pad. Animals recovered within 1 h after the end of the scan. Two of the 4-months old TgF344-AD rats did not recover after the scan due to premature extubation.

## 2.3. Preprocessing

The data underwent pre-processing that included debiasing, normalization, realignment, smoothing, and co-registration, all facilitated by the SPM12 software suite (Statistical Parametric Mapping). Initially, to mitigate the smooth intensity gradient variations caused by the RF coil reception, debiasing was applied to the 3D RARE scans. Subsequently, a custom 3D template was created from these corrected scans (4 m 11WT/15AD, 6 m 11WT/13AD) using Advanced Normalization Tools (ANTs). This template was generated using a global 12-parameter affine transformation followed by a non-linear deformation process, minimizing deformation as criterion. All individual 3D scans were then aligned to this template via a similar global affine transformation. For the rs-fMRI images, realignment to the initial image was achieved through a 6-parameter rigid body transformation, calculated by the least squares method. These images were then co-registered to the anatomical 3D scans from the same session, employing a 12-parameter affine transformation that utilized mutual information as the metric for similarity. The parameters obtained from aligning the 3D scans to the template were then applied to all rs-fMRI images. In addition, signals from white matter, ventricles, and the overall global signal were regressed from the rs-fMRI data. In-plane smoothing was performed using a Gaussian kernel, with full width at half maximum (FWHM) equal to twice the voxel size. To conclude, the initial and final 10 images of the

pre-processed rs-fMRI scans were discarded. The remaining images were then subjected to temporal bandpass filtering within the frequency range of 0.01 to 0.17 Hz designed to avoid frequencies induced by the ventilator.

## 2.4. Methods

An overview of the analysis of the rs-fMRI data using the RP method is shown in Fig. 1. In this *in-vivo* study, the goal was to use RQA analysis as a potentially more sensitive approach that can identify non-linear dynamical changes in brain function as a result of very early time-points of AD and the effects of longitudinal changes over time (aging). Consequently, identifying such patterns can lead to diagnosis of early AD by revealing the affected brain regions and specific changes to look for in AD subjects. After motion registration and primary data pre-processing (see Materials) of rs-fMRI data of TgF344-AD (AD, N = 13) and wild-type rats (WT, N = 11), all voxels of areas associated to the default mode-like network (DMLN) were selected based on the Fischer344 atlas [49]. The DMLN, is a large-scale network of brain regions co-activated during rest and throughout self-referential mental activities and cognitive tasks [50]. Given that this network has shown changes and deterioration in AD, this study focused specifically only on the DMLN regions. First, a recurrence plot from individual voxels of the DMLN was obtained, and then utilizing the RQA method for each voxel of the rs-fMRI scans, the variations of different measures, including entropy of the diagonal line (ENT), recurrence rate (RR), determinism (DET) and average diagonal line (ADL), were statistically analyzed in two groups (AD, WT) and two ages (4- and 6-months old).

## 2.5. Voxel time series extraction and default mode like network

Our data included four classes: 1) TgF344-AD rats at four months of age, (AD\_4m). 2) TgF344-AD rats at six months (AD\_6m). 3), Wild-type F344 rats at four months (WT\_4m). 4) Wild-type F344 rats at six months (WT\_6m). All voxels of the regions of interest (ROI) were extracted based on the Fischer344 atlas labels [49]. One hundred and seventy matrices ( $Ni^*BOLD$  i=1, 2...,170) were made for each subject, where  $Ni$  is the number of voxels for each ROI, and BOLD signals are the 980-point time series (TR=600 ms, total time=9.8 min) of the rs-fMRI data for each voxel.

Initially, a whole brain RQA was performed at the ROI level, but not many significant differences between the groups were observed. Then, our study focused only on the rat brain at the voxel level and specifically in the DMLN, which includes the hippocampal fields (CA1, CA2, CA3), the primary (V1) and secondary visual cortex (V2), the retrosplenial cortex (RSC), the orbitofrontal cortex (OFC), prelimbic (PrL) and infralimbic cortices (IL), temporal association cortex (TeA), the cingulate cortices (CG1, CG2), parietal association cortex (Pta) and the basal forebrain (BFB). Table A1, in the appendix, shows the names and abbreviations of the DMLN regions based on the Fischer344 atlas.

## 2.6. Recurrence plots

In order to outline the key ideas and theories that help us understand recurrence plots, first, we need to define a recurrence in dynamic systems. Suppose we have a system  $s$ ; in time  $t_i$ ,  $s$  has the state  $x(t_i)$ , and in time  $t_j$ ,  $s$  has the state  $x(t_j)$ ; if  $x_i$  and  $x_j$  are similar enough, there is a recurrence in times  $i$  and  $j$ . The similarity between  $x(t_i)$  and  $x(t_j)$  is enough to warrant a recurrence when the absolute difference of the two states is less than a threshold  $\epsilon$ . A recurrence plot of  $s$  depicts all the instances in which a recurrence has occurred. We can obtain a recurrence plot with the following equation:

$$T = \langle t_1, t_2, \dots, t_n \rangle \quad (1)$$

$$X = \langle x(t_1), x(t_2), \dots, x(t_N) \rangle \quad (2)$$

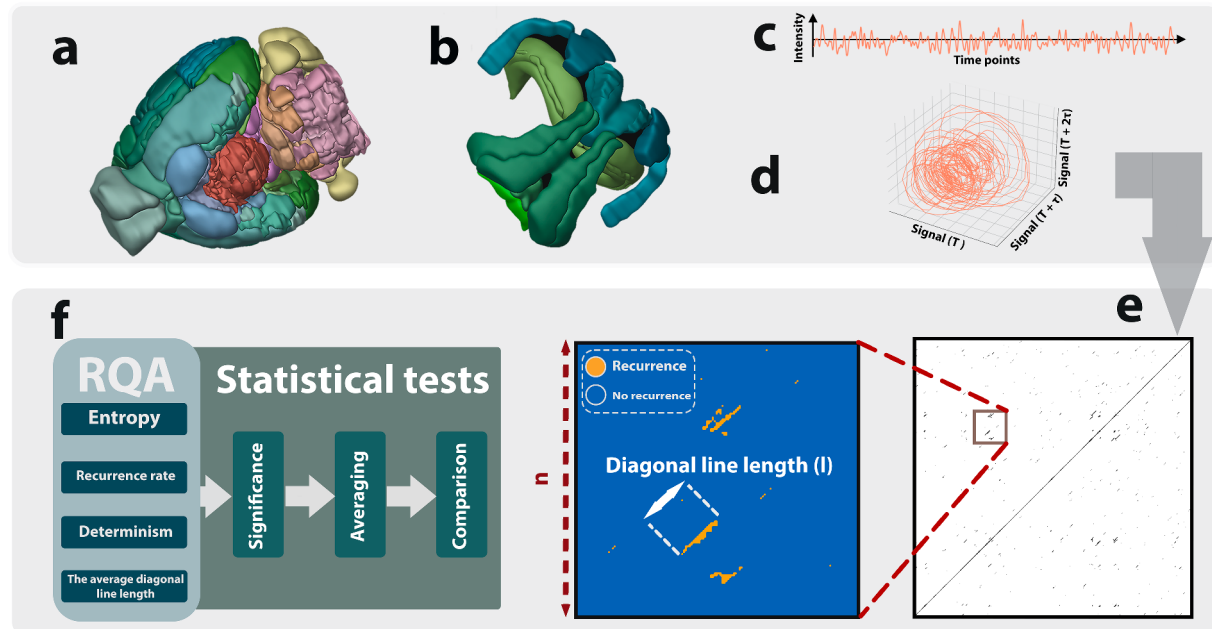


**Fig. 1.** Overview of the proposed framework for analysis of the rs-fMRI data using the RP method. (a) longitudinal rs-fMRI sessions of TgF344-AD rats (AD,  $N = 13$ ) and wild-type (WT,  $N = 11$ ) at four and six months of age. A 3D image of all regions of the rat brain is depicted using the Allen atlas and the brain explorer software [51,52]. (b) In this study, only the DMLN areas were considered for further investigation. These regions include the hippocampal field, primary and secondary visual cortices, retrosplenial cortex, and cingulate cortex. (c) All voxels of the DMLN were extracted based on the Fischer344 atlas. (d) Applying the estimated optimal time delay, dimension, and threshold, the phase space trajectories for all voxels' time series of the DMLN regions were reconstructed. Here a trajectory is depicted in 3 dimensions with each one representing the original time series signal delayed by a factor of the time delay ( $\tau$ ). (e) Using the reconstructed trajectories, a recurrence plot per voxel is generated for the DMLN. The middle plot (blue and yellow colored) illustrates an enlarged part of the RP. In this figure each recurrence is depicted as yellow points and all other states as blue points. Here  $n$  is the number of time points in this section of the RP and  $l$  is the diagonal line lengths. (f) After constructing the RPs, several quantitative features are extracted from recurrence plots using the RQA method to interpret the recurrence patterns and provide more in-depth information. Next, those voxels with a p-value (obtained using permutation test) smaller than 0.05 are selected. The average of the relevant parameter of the significant voxels is calculated for all subjects in each class to compare the 4-months and 6-months old rats in WT and AD groups.

$$R(i,j) = \begin{cases} 1, & |x(t_i) - x(t_j)| \leq \epsilon \\ 0, & \text{Otherwise} \end{cases} \quad (3)$$

Eq. (1), is the set of time points in the time window  $T$  where the system is active. In Eq 2,  $X$  is the set of the system's considered states and Eq 3 is the Heaviside function in which there is a recurrence where the difference between the two states of the system is less than  $\epsilon$ . The structural patterns in RPs contain information on the evolution of the system trajectories. There are three small scale structures in an RP: single points which appear if states are infrequent, a diagonal line which takes place when a segment of the trajectory moves parallel to another, and a vertical or horizontal line that shows a prolonged change or no change at all [53].

Before calculating recurrence plots from a time series, first, we need to reconstruct the trajectory of the time series in the phase space. Taken's theorem has shown that such reconstruction is possible using the time delay embedding method [54,55]. This theorem declares that a time series  $x_1, x_2, \dots, x_N$  sampled from a higher dimensional attractor can be reconstructed via delay embedding as follows:

$$\langle x(t_i), x(t_i + \tau), \dots, x(t_i + (D-1)\tau) \rangle \quad (4)$$

$$i = 1, 2, \dots, N - (D-1)\tau \quad (5)$$

where  $t_i$  is a time point in the time series,  $\tau$  is the time delay, and  $D$  is the embedding dimension. Therefore, the first step is to determine how much delay our time series needs in the phase space along with how many dimensions the system must be reconstructed into.

## 2.7. Time delay

The first parameter for trajectory reconstruction is the time delay ( $\tau$ ). It is obtained by minimizing the interaction between points of the time series. Optimal time delay is calculated using average mutual information (AMI) [56]. Mutual information, a concept from information theory, measures the mutual dependence between two variables by quantifying the amount of information obtained by one variable by observing the other [27]. The AMI of time series  $x(t)$  and the delayed time series  $x(t + \tau)$ , can be calculated by the following equation [57]:

$$I(x(t), x(t + \tau)) = \sum_{ij} p_{ij}(\tau) \log \left( \frac{p_{ij}(\tau)}{p_i p_j} \right) \quad (7)$$

Here  $I$  denotes the mutual information of the time series,  $p_i$  represents the probability that  $x(t)$ , falls within the  $i$ th bin of the histogram of the data, and  $p_{ij}(\tau)$  represents the probability that  $x(t)$  belongs to bin  $i$  while  $x(t + \tau)$  belongs to bin  $j$ . First, the time series is delayed by  $\tau$ ; next, AMI is calculated to see how much information is shared between the non-delayed and the delayed time series. This procedure is repeated for multiple values of  $\tau$ , and, finally, the local minimum is chosen as the optimum time delay [58] so the independence of the two time series is maximized. In this paper, we calculate a recurrence plot for each voxel of the DMLN areas in the rs-fMRI data. Given a sufficiently large dimension, the time delay is a non-critical parameter, meaning that its changes will not greatly affect measurable characteristics of the system; therefore, many values of time delay can serve as a local optimum for that system [59]. We have estimated the optimum  $\tau$  for all voxel's time series of the DMLN regions using the AMI approach by choosing the minimum value [60].

## 2.8. Dimension

The next step is to determine the dimension of the reconstructed trajectory known as the embedding dimension. A too small embedding dimension results in false recurrences. One popular method for embedding dimension estimation for experimental data is the false nearest neighbors (FNN) method [56]. FNN determines if two points in dimension  $D$  and  $D + 1$  are true or false neighbors. Two points are considered neighbors if they are in close proximity, meaning they have a small difference in magnitude [57]. A false neighbor is a pair of points in the time series that we see as neighbors in the reconstructed trajectory due to the small embedding dimension. As  $D$  increases, the number of FNNs decreases. The first  $D$  value in which the number of FNNs is zero [61], when the system's information is maximized, is selected.

In a  $D$ -dimensional phase space, the squared Euclidian distance between coordinates  $x$  and its  $r$ th nearest neighbor is:

$$R_D^2(t, r) = \sum_{k=0}^{D-1} [x(t_i + k\tau) - x^r(t_i + k\tau)]^2 \quad (8)$$

where  $x^r(t_i + k\tau)$  is the  $r$ th nearest neighbor of  $x(t_i + k\tau)$ . If  $D$  is increased by one to reconstruct  $D+1$ -dimension phase space through time delay embedding, the distance between  $x(t_i + k\tau)$  and  $x^r(t_i + k\tau)$  is given by:

$$R_{D+1}^2(t, r) = R_D^2(t, r) + [x(t_i + D\tau) - x^r(t_i + D\tau)]^2 \quad (9)$$

Since we only add one extra dimension,  $x(t_i + D\tau)$ , the new squared distance is the sum of the squared distances of the previous dimensions and squared distances of the new dimension. If the distance between two coordinates increases significantly after going from  $D$ -dimensional space to  $D + 1$ -dimensional space, then the two points are false neighbors. This can be described by the following equation:

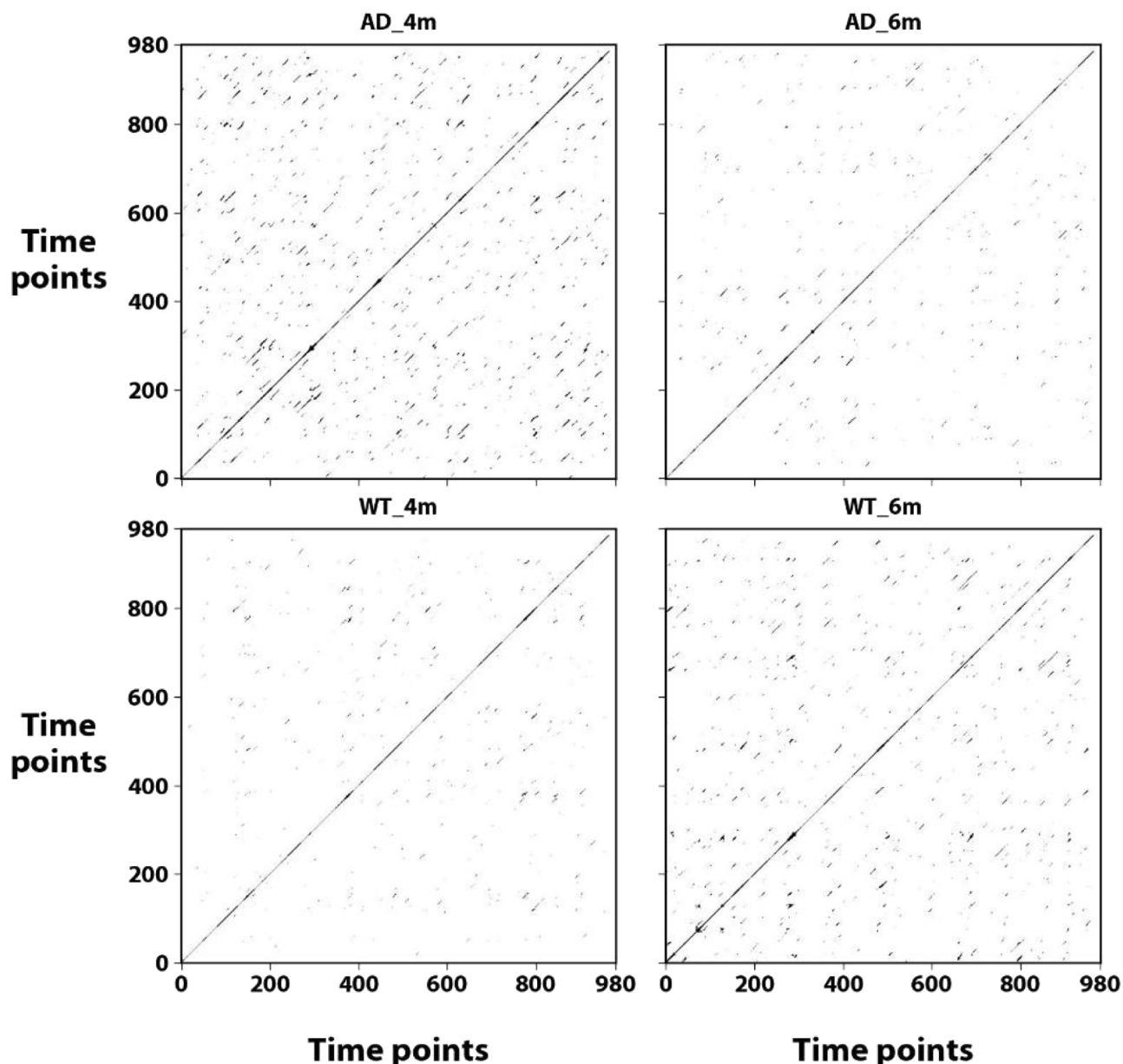


**Fig. 2.** Recurrence plots of a single voxel in the CA1 region for one rat in each data class. RPs were calculated with the optimal time delay, dimension, and threshold reported in table 1.

$$\sqrt{\frac{R_{D+1}^2(t_i, r) - R_D^2(t_i, r)}{R_D^2(t_i, r)}} = \frac{|x(t_i + D\tau) - x^r(t_i + D\tau)|}{R_D(t_i, r)} > R_{tol} \quad (10)$$

$$i = 1, 2, \dots, N - D\tau \quad (11)$$

Where  $R_{tol}$  is the tolerance threshold. The main drawback of the FNN algorithm is the need for an optimal choice of  $R_{tol}$ . The Average False Neighbors (AFN) method addresses this by averaging all the distances for dimensions  $D$  and  $D+1$  and calculating the ratio of the average distances of  $D+1$  and  $D$  [62]. The below equations describe these operations:

$$E(D) = \frac{1}{N - D\tau} \sum_{i=1}^{N-D\tau} a(t_i, D) \quad (12)$$

$$E1(D) = \frac{E(D+1)}{E(D)} \quad (13)$$

$a(t_i, D)$  is the maximum norm form of Eq. (10).  $E1(D)$ , stops changing when  $D$  surpasses some value  $D_0$ , when this occurs the optimal dimension is noted as  $D_0 + 1$ .  $E1(D)$  is only dependent on  $D$ , therefore there is no need for the choice of heuristic parameters such as  $R_{tol}$ .

We have calculated  $D$  for each voxel's time series and selected the most frequent dimension in all of our data [63]. Estimating optimal time delay and embedding dimension were done using NeuroKit2, a python-based toolbox [64]. The final step is to determine the optimal threshold  $\varepsilon$ . If  $\varepsilon$  is too high or too low, the number of recurrences increases or decreases, respectively, to a level with no distinguishable features in the plot. There are few methods for choosing the optimal  $\varepsilon$ . Here, we have selected a threshold of 10 % of the mean phase space diameter (PSD) of the reconstructed trajectory [63,65]. After obtaining the optimal time delay, dimension, and threshold, a recurrence plot per voxel was generated from each voxel's time series using the Cross Recurrence Plot (CRP) Toolbox [56,66] and MATLAB. Fig. 2 shows the recurrence plots of the same voxel in the hippocampal CA1 region of four rats in each class.

## 2.9. Recurrence quantification analysis (RQA)

It is considered that quantitative features would complement our insights in interpreting patterns and structures provided by the recurrence plot. Hence, in an attempt to capture the complexities of RPs and obtain further in-depth information, a quantitative approach referred to as Recurrence Quantification Analysis (RQA) was employed since the early 1990s by Zbilut and Webber to quantify the small-scale structures in the RPs [67]. RQA features are based on the recurrence point density of the diagonal and vertical line structures of RPs [56]. The present study focuses on four features that function as complexity measures.

### 2.9.1. Entropy of the diagonal line (ENT)

Assume that in an RP,  $l$  is the length of a diagonal line, and  $p(l)$  is the likelihood of finding a diagonal line of length  $l$ . Therefore, the diagonal line's entropy, which in turn indicates the complexity of the RP with regard to the diagonal lines, is defined as the Shannon entropy of  $p(l)$  (ENT) [27]. ENT may be thought of as a measurement of the amount of information needed to retrieve the system and is determined as follows:

$$ENT = - \sum_{l=l_{min}}^N p(l) \log(p(l)) \quad (14)$$

where  $N$  is the number of time points in the voxel time series. Lower ENT values imply a random state or noise, whereas higher levels indicate a periodic behavior.

### 2.9.2. Recurrence rate (RR)

The second measure in RQA is recurrence rate (RR) which relies on

the recurrence point density. RR calculates the ratio of recurrence states to all states. The range of values for RR is 0 to 1, with 0 suggesting unpredictable behavior and 1 indicating a stable signal. The RR is computed as follows:

$$RR = \frac{1}{N^2} \sum_{i,j=1}^N R_{i,j} \quad (15)$$

where  $N$  is the number of time points in the voxel time series and  $R_{i,j}$  is a recurrence between the times  $i$  and  $j$ .

### 2.9.3. Determinism (DET)

The ratio of recurrence points forming a diagonal line to all other recurrence points in the RP is known as determinism (DET). Short diagonal lines and lower DET values are indicators of a chaotic and unpredictable signal. Systems with particular patterns, on the other hand, will produce longer diagonal lines and larger DET values. This metric is obtained with Eq. (16):

$$DET = \frac{\sum_{l=l_{min}}^N lp(l)}{\sum_{l=1}^N lp(l)} \quad (16)$$

$N$  is the number of diagonal lines,  $l$  is the length of a single diagonal line, and  $p(l)$  is a histogram of diagonal lines with a length of 1.

### 2.9.4. The average diagonal line length (ADL)

A diagonal line length demonstrates that the system has substantially identical states from the start to the end of the line; in other words, the system is stationary during that period. We can conclude that diagonal lines represent system divergence, thus greater average diagonal line length (ADL) suggest a predictable system [56]. The average diagonal line length is defined as:

$$ADL = \frac{\sum_{l=l_{min}}^N lp(l)}{\sum_{l=l_{min}}^N p(l)} \quad (17)$$

To study the variation of RP in WT and AD rat models, we have calculated the four aforementioned features for each voxel in the DMLN areas. Next, a statistical analysis is performed to assess if the differences of each measure between the two groups are significant. Such statistical testing is necessary to ensure that the RQA method can distinguish between AD and healthy rats and other classes with a high level of certainty. For this goal, the permutation test with 10,000 resamples was utilized. In this study, the threshold level (alpha) was set to 0.05. For each voxel, we check if there is a significant difference between the following four cases: 1) AD\_4m and WT\_4m, 2) AD\_6m and WT\_6m, 3) AD\_4m and AD\_6m, and 4) WT\_4m and WT\_6m. The statistical comparison between many voxels rises major problems in decision making and interpretations with p-values due to the existence of false positives. Permutation methods are one of the approaches of controlling the family-wise error rate (FWER), which does not require any assumption about the distribution of data. Under the null hypotheses, there are no statistical differences between the two groups.

After permutation testing, those voxels with a p-value smaller than alpha (=0.05) are selected. Next, for each feature, the average value of the remaining voxels for all subjects in each class is computed. Finally, the obtained average values for the same voxel in two different groups are subtracted. The mathematical description of these operations is shown in Eqs. (18)–(21):

$$F = \{ENT, RR, DET, ADL\} \quad (18)$$

$$C = \{AD\_4m, AD\_6m, WT\_4m, WT\_6m\} \quad (19)$$

$$\bar{f} = \frac{\sum_{i=1}^{N_R} f(v_i)}{N_R} | f \in F \quad (20)$$

$$\Delta\bar{f} = \bar{f}_{c_i} - \bar{f}_{c_j} \mid c_i, c_j \in C \quad (21)$$

$F$  is the set of RP features,  $C$  is the set of classes,  $\bar{f}$  is the average value of the feature  $f$ ,  $v_i$  is a significant voxel,  $f(v_i)$  is the value of the feature  $f$  for  $v_i$ ,  $N_R$  is the number of subjects in each comparison (13 for AD and 11 for WT) and  $\Delta\bar{f}$  is the difference between the class  $c_i$  and  $c_j$  for feature  $f$ . We calculate  $\Delta\bar{f}$  for all significant voxels in the DMLN. The order of the subtraction is AD-WT and 4m-6 m. In other words, positive/negative values show that for that specific feature we have higher/lower values either in the AD group or the younger subjects depending on the test. An overview of the proposed framework is illustrated in Fig. 1.

### 3. Results

#### 3.1. Parameter values to construct RPs

The first step in RQA analysis, was to select the optimal time delay ( $\tau$ ), dimension, and phase space diameter (PSD), the diameter of the reconstructed trajectory in phase space. Fig. 3 shows the distributions of these parameters for each voxel's time series in the DMLN areas across all rats. The time delay  $\tau$  is measured in discrete time points of the rs-fMRI data as each time point corresponds to one TR (0.6 s), the sampling rate of the fMRI imaging. Using the AMI method, the optimal  $\tau$  for each voxel was estimated as the minimum  $\tau$  across all voxels, in this case  $\tau=3$  TRs, which is equivalent to 1.8 s (Fig. 3a). Next, the optimal dimension for each voxel's time series was determined utilizing the AFN algorithm. This was 6 (Fig. 3b), and thus it was chosen for reconstruction of the trajectories. In order to find the optimal threshold ( $\epsilon$ ), the PSD for all voxels was measured using the CRP Toolbox to select 10 % of the mean PSD as  $\epsilon$ . This resulted in an optimal threshold  $\epsilon=9.16$  (Fig. 3c). Table 2 summarizes these estimates. In addition, as a control, RQA analysis was performed on the same subjects with  $\epsilon=4.58$  (5 % of mean PSD) and the results are presented in the appendix in Figs. A1 and A2.

#### 3.2. AD-phenotype related changes in RQA parameters of rs-fMRI data at 4- and 6-months

To examine the alterations in the brain caused by the AD phenotype in TgF344-AD versus WT F344 rats, we analyzed the rs-fMRI signals using the RP method in our longitudinal, two-timepoint study. From the RPs, we calculated the non-linear features described by Eqs. (14)–(17), specifically: 1) entropy of the diagonal line (ENT), 2) recurrence rate (RR), 3) determinism (DET), and 4) average diagonal line length (ADL).

**Table 1**

Selected parameters to construct the recurrence plots for each voxel time series. These parameters are fixed for AD and WT groups and 4 m and 6 m old rats.

| Parameter | Time delay ( $\tau$ ) | Dimension ( $D$ ) | Threshold ( $\epsilon$ ) |
|-----------|-----------------------|-------------------|--------------------------|
| Value     | 3 TRs<br>(1.8 s)      | 6                 | 9.16                     |

Then, using permutations for identifying voxels with significant differences and Eqs. (18)–(21) we estimated the average differences of these parameters across the AD and WT rats. To identify whether there is progression of identified changes across the two timepoints (4 m and 6 m), this analysis was performed per timepoint. Fig. 4 depicts the results of the RQA approach between AD\_4m – WT\_4m and AD\_6m – WT\_6m groups. Each circle in Figs. 4a to 4d corresponds to a voxel in the DMLN that had statistically significant changes between the compared groups. The green circles indicate the differences of each RP measure in the rats at 4-months and the red circles illustrate the same at 6-months of age. The black lines represent the mean of a feature in a specific DMLN brain region (see labels on the x-axis). Fig. 4a shows the differences of ENT between AD and WT. At 4-months of age (green circles) a decrease of ENT was observed in the AD group relative to the WT group in the BFB, CA1, and CA3 regions while the reverse (an increase in AD) was found for the primary and secondary visual cortices albeit with more variability across voxels. This is evident as the differences of ENT are exclusively negative for BFB, CA1 and CA3 and mostly positive for V1 and V2. In the PtA, although several voxels were significant, both increases and decreases were observed and thus it showed only a slightly positive mean  $\Delta\text{ENT}$ . Interestingly, at 6-months of age, we didn't observe a simple progression of these changes but instead a quite different pattern. Specifically, except for a single voxel in the CA1 region, all other  $\Delta\text{ENT}$  values were positive indicating increases of ENT in the AD group. Indeed, at this older age group, the changes observed did not simply follow a progression or worsening of the pattern observed at 4 months but instead a different pattern emerged (Fig. 4a, red circles), indicating that the brain may respond to initial changes reversing their directionality. At the 6-months timepoint, AD phenotype rats showed in most areas - including BFB, CA1, CA3, that exhibited decreases at 4-months, increased entropy compared to the WT group. Moreover, other regions such as CG2, PrL, PtA, and RSC also showed a consistently increased ENT in contrast to 4-months. In the visual cortex (V1, V2) where an increased ENT was already observed at 4 m, the increases also became more consistent in V2; However, in V1 there was a rise in the number of significant voxels but the mean  $\Delta\text{ENT}$  was slightly lower in

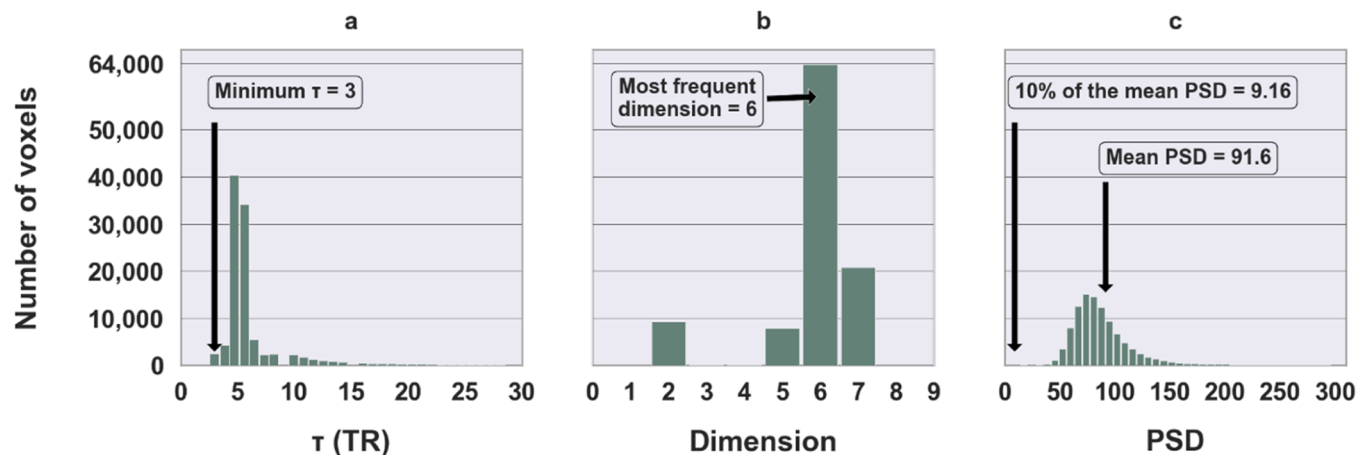


**Fig. 3. Distribution of time delay, dimension, and phase space diameter of all voxels across all subjects.** In the time delay and PSD estimation, outliers with high values (above 30 and 300 respectively) were discarded on these figures. (a) Using the AMI algorithm,  $\tau$  is estimated for all voxels. The minimum  $\tau=3$  is selected as the optimal time delay. (b) applying the AFN method to the DMLN voxels show the most frequent dimension to be 6. (c) by measuring the diameter of the reconstructed trajectories in phase space, and considering 10 % of the mean diameter of all voxels,  $\epsilon=9.16$ , is selected.

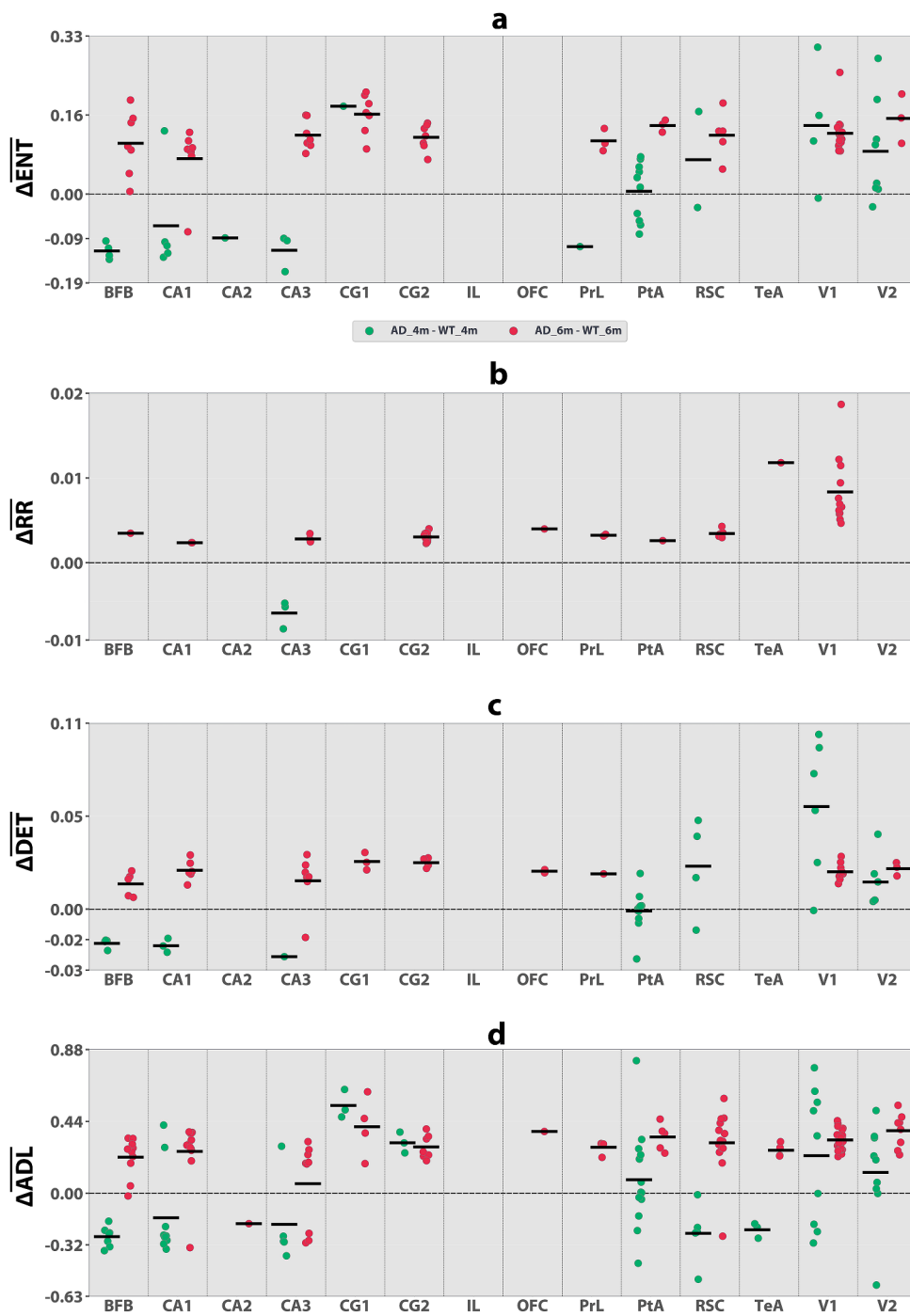


**Fig. 4. Results of the comparison between AD and WT rats at 4- and 6-months old using the RQA method in the DMLN regions.** Green\red circles represents comparison at 4\6 months old and the black lines indicates the mean value of the features in a specific region. (a) The differences of ENT in AD<sub>4m</sub> – WT<sub>4m</sub> and AD<sub>6m</sub> – WT<sub>6m</sub>. At 4 months, the BFB, CA1 and CA3 present with higher ENT values in the WT rats while PtA, V1 and V2 had greater values in the AD rats as the subtraction of AD – WT are primarily positive. As the rats grew, in most regions, ENT increased for the AD rats as the red circles have higher means than the green ones. The opposite is true for the CG1 and V1 regions. (b) The differences of RR in AD<sub>4m</sub> – WT<sub>4m</sub> and AD<sub>6m</sub> – WT<sub>6m</sub>. RR shows greater values for AD subjects at 6-months old, yet no apparent alteration in the younger rats except for the CA3 region. (c) The differences of DET in AD<sub>4m</sub> – WT<sub>4m</sub> and AD<sub>6m</sub> – WT<sub>6m</sub>. Here, similar patterns to ENT are observed. However, at 6-months old, DET did not detect any neural activity changes of RSC and PtA. (d) The differences of ADL in AD<sub>4m</sub> – WT<sub>4m</sub> and AD<sub>6m</sub> – WT<sub>6m</sub>. In addition to the neural patterns observed in Fig. 4.a, ADL detected the effects of AD at both ages in the TeA and CG2 regions. These changes indicate the growth of ADL in TeA, and the decrease of the measure in CG1 and CG2 with age in the diseased rats. BFB: basal forebrain, CA1: hippocampal field 1, CA2: hippocampal field 2, CA3: hippocampal field 3, CG1: cingulate cortex area 1, CG2: cingulate cortex area 2, IL: infralimbic cortex, OFC: orbitofrontal cortex, PrL: prelimbic cortex, PtA: parietal association cortex, RSC: retrosplenial cortex, TeA: temporal association cortex, V1: primary visual cortex, V2: secondary visual cortex.

the older rats.

**Fig. 4b**, demonstrates the differences of RR in AD and WT rats. As apparent from the figure, this feature did not detect any changes in the younger 4 m group except for three voxels in the CA3 region. Instead, the 6 m old rats (red circles) showed positive differences demonstrating higher RR values in the AD rats at this age. **Fig. 4c-d** present the values for the DET and ADL measures respectively. These two parameters showed similar patterns to ENT (compare to **Fig. 4a**). However, some differences were also apparent e.g., significant differences were only present for  $\Delta\overline{DET}$  in RSC and PtA only in the 4 m rats. The ADL results are presented in **Fig. 4d**. CG1 and CG2 showed increases irrespective of age, thus on this feature significant changes in CG1, CG2 could already be detected at 4 m. Moreover, in the younger rats, the RSC region had lower  $\Delta\overline{ADL}$  values in the AD rats, suggesting a more stationary trajectory of brain signals in this region for the healthy rats. ADL also revealed that in the primary visual cortex at 4 m the changes were variable but became very consistently positive at 6 m. Furthermore, ADL is the only measure that detects changes in AD across both ages in the TeA region, albeit with reverse polarities suggesting that as the rats grew, the diseased group has more deterministic neural activity in this region compared to when they were 4 m old. As the same pattern was observed across 3 of the 4 measures (ENT, DET and ADL) in other regions including the BFB, CA1, and across ages, this could support some unknown compensatory mechanisms in the brain kicking in after the initial changes at 4 m.

### 3.3. Age related changes in RQA parameters of rs-fMRI data of AD and WT rats

Given that in the previous section changes in the AD group were always compared with the WT group at the same age, it was not clear how the parameters in each of the two groups evolve over time across the two age groups. Thus, here we performed a similar analysis but comparing instead of phenotypes the differences in each group across the two ages. **Fig. 5** summarizes the findings of this analysis. Yellow circles represent the values for the AD\_4m – AD\_6m comparisons and the blue circles show the same for the WT rats at 4- and 6-months. In general, going from 4 m to 6 m in both groups, we observed on average, decreases in all 4 parameters (i.e., higher values in 4 m AD or WT animals). This indicates an overall reduction in determinism and predictability over time. Regarding ENT (**Fig. 5a**), we observed robust changes in healthy rats (blue circles) across many areas (BFB, CA1, PrL, PtA, RSC and V2). Interestingly, age had a less prominent effect in the AD rats (yellow circles) as very few voxels had any statistically significant differences between the two-age groups. This effect was even more pronounced for RR (**Fig. 5b**), as for this parameter we only observed robust differences for the WT group. For DET, we observed analogous finding to ENT (**Fig. 5c**), albeit one intersecting dissimilarity was the negative means of DET in the V1 and V2 areas. Notably, results for ADL were also similar (**Fig. 5d**), but more significant voxels were detected in the AD group for this parameter indicating that it is an important and sensitive measure that can detect subtle changes. All significant regions exhibit positive means; However, the WT group is clearly more consistent while for the AD group there is greater variability within the voxels showing both increases and decreases. Higher ADL implicates a dynamical system with more stationary behavior. This suggests a sharper decline of ADL for the younger rats of the WT group. Thus, over time, the neural activity of these regions in the WT rats became less static and predictable. While the same was true for the AD subjects in most regions, this decline in predictability was less prominent.

## 4. Discussion

This study examined the changes in brain activation patterns represented in rs-fMRI data of 4- and 6-month-old TgF344-AD and WT

littermate rats. To achieve this, we employed the RQA method, a non-linear approach that identifies recurrences of states in a dynamic system. We hypothesized that RQA can effectively detect subtle changes missed by other methods due to the non-linear nature of the brain. To this end, we constructed RPs from the rs-fMRI images and obtained four RQA feature parameters, ENT, RR, DET, and ADL. We found that all four RQA parameters detected alterations because of the AD phenotype in transgenic rats as well as over time across the age groups. Across the four parameters, RR seemed to underperform in comparison to the other selected measures, while ADL seemed to be the most sensitive of the four. Nevertheless, all measures can be extracted from the same analysis and their power could be combined in case of development of biomarkers for detection and classification in specific disorders. Our results demonstrate that RP and RQA can be used as a novel tool in characterizing changes in brain function both in diseases such as AD as well as to detect changes during development.

Using the RQA approach we identified significant changes related to the AD phenotype at 4 m and/or 6 m in several areas of the rat DMLN including the BFB, Hippocampal fields CA1 and CA3, CG1, CG2, PrL, PtA, RSC, TeA, V1, V2. Previous studies have shown that the basal forebrain in humans is affected in patients with MCI and AD [68–70]. Consistently, we have recently used quasi-periodic pattern (QPP) analysis and have shown in the same rats as used in the current study reduced activity in the basal forebrain and parts of the DMLN at 4 m of age [48]. At 6 m of age, however, the differences between the two groups were less abundant, which led us to suggest that possible compensation mechanisms are at play at this age [48]. Similar findings were also observed using co-activation pattern (CAP) analysis [71]. The results of our current study, go a step beyond this previous work by showing consistent changes in multiple areas at the 6 m timepoint, indicating that the RQA approach is more sensitive to subtle changes.

Furthermore, CA1 and CA3 are key regions involved in memory functions and learning. A recent study revealed vulnerabilities of these regions to the amyloid-beta protein [72]. Other researchers, found disrupted synaptic plasticity in the visual cortex of rats with tauopathy, a disorder that results in deposition of the tau protein in the brain [73]. Consistent with these findings, our results also showed differences of RQA measures in these regions between AD and WT rats. By comparing the RQA features we identified key brain regions that were affected by AD at the pre-clinical stage, including, hippocampal CA1, CA3, basal forebrain, and the primary and secondary visual cortices as they were the regions with most differences between AD and the control group. Moreover, we found that at 6 m, the differences of ENT, DET and ADL across AD and WT rats, reverse direction from negative to positive in the basal forebrain and the hippocampus. This switch could indeed relate to a potential compensatory mechanism in the brain to counter the effects of AD but importantly using this analytic approach, changes remain detectable also at this timepoint.

In addition, we observed differential effects of developmental age on brain activity in AD and WT rats using RQA features. Notably, our findings revealed that when modeling the brain as a dynamical system, a reduction of the system's predictability occurs in both healthy and diseased rats. However, in AD rats this reduction was to a lesser extent, which could implicate pathological processes. Wang et al. have found that brain entropy increases with normal aging in a cross-sectional human rs-fMRI study. In contrast, they showed that brain entropy increases slightly during SMC and then drops as the disease progresses into AD [74]. In other words, the predictability of brain function diminishes, and chaos increases as individuals age normally, whereas the opposite trend is observed in patients with AD. In this longitudinal study, our findings support these results by further demonstrating that at the pre-clinical stage, the brain will in fact behave more chaotically and become less predictable with aging in healthy and AD rats; however, the growth of the non-predictability is less acute in the AD group. Given the results of this study, and the fact that RQA was able to discover key insights into the early stages of AD, we can conclude that this method

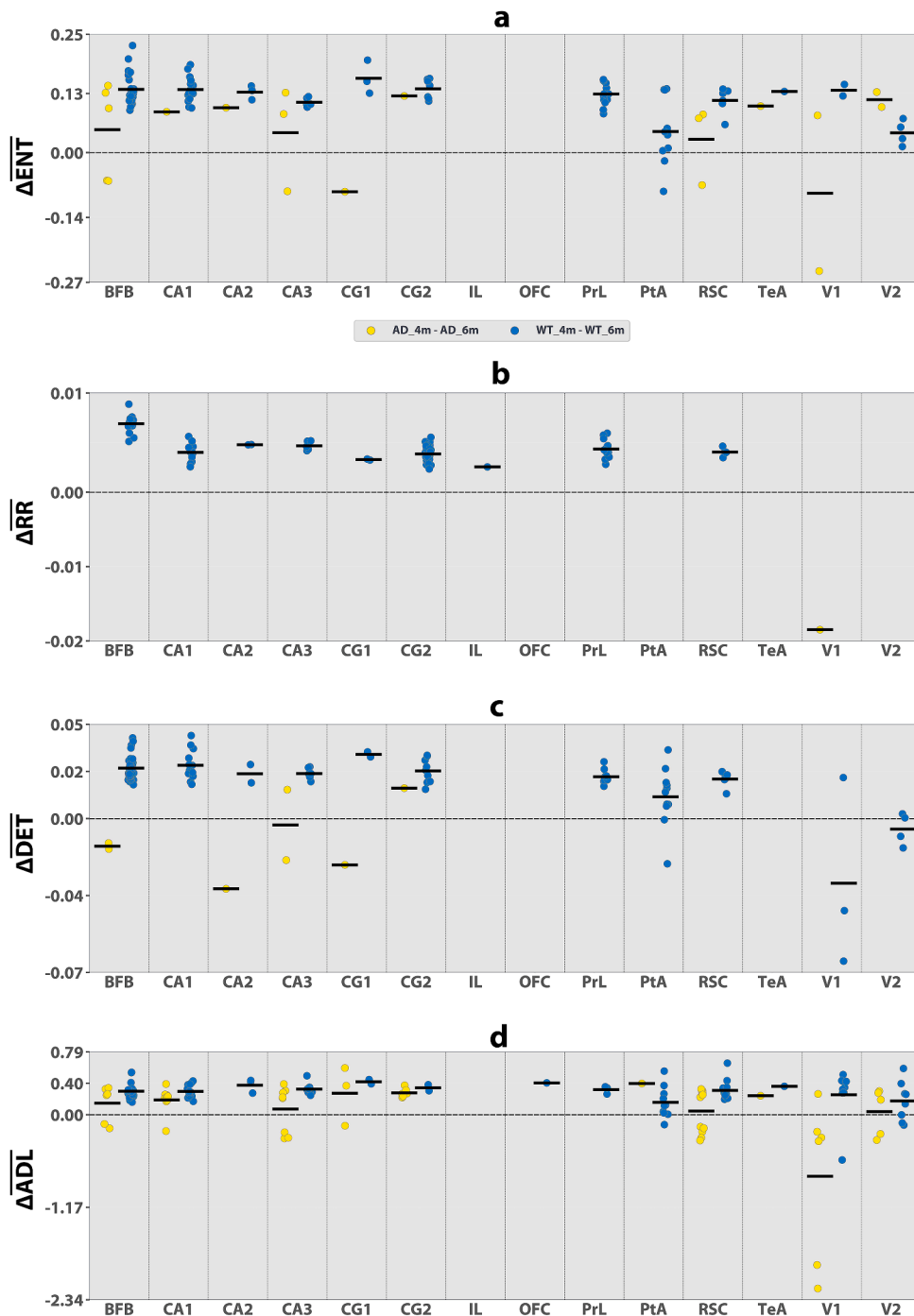


**Fig. 5. Results of the comparison between 4-and 6-months rats using the RQA method in the DMLN regions.** Yellow/Blue circles represents comparison of AD \WT groups and the black lines indicates the mean value of the features in a specific region. (a) The differences of ENT in AD\_4m – AD\_6m and WT\_4m – WT\_6m. ENT can in fact detect the effects of aging in both rat groups. Important regions include the BFB, CA1, PrL, RCS and V2. These alterations are less apparent in the AD rats. Most regions in both groups suggest higher ENT values for the younger rats with positive means (b) The differences of RR in AD\_4m – AD\_6m and WT\_4m – WT\_6m. RR only detects brain alterations due to aging in the WT rats. (c) The differences of DET in AD\_4m – AD\_6m and WT\_4m – WT\_6m. Similar findings to ENT can be observed here. Except for the V1 region, which has lower DET values at 4-months in the healthy rats. (d) The differences of ADL in AD\_4m – AD\_6m and WT\_4m – WT\_6m. Comparison of ADL values reveals that as the rats grow up, their brain activity in most regions morphs into a less stationary dynamical system. This is evident from the figure as almost all regions in both AD and WT subjects have positive means. In other words, the subtraction of ADL values is positive indicating that the younger subjects had a higher ADL value therefore a more predictable behavior. However, this pattern is less strong in the AD rats as they demonstrate lower means than the WT rats BFB: basal forebrain, CA1: hippocampal field 1, CA2: hippocampal field 2, CA3: hippocampal field 3, CG1: cingulate cortex area 1, CG2: cingulate cortex area 2, IL: infralimbic cortex, OFC: orbitofrontal cortex, PrL: prelimbic cortex, Pta: parietal association cortex, RSC: retrosplenial cortex, TeA: temporal association cortex, V1: primary visual cortex, V2: secondary visual cortex.

has the potential to be used in clinical and diagnostic studies in the future.

## 5. Conclusion

In this study, to observe the effects of AD and aging in 4- and 6-month-old TgF344-AD and Wild type rats, we applied the recurrence quantification analysis method to rs-fMRI signals focusing on the DMLN regions of the brain. In this way, we found several brain regions significantly impacted by AD, notably the Basal forebrain, Hippocampal fields CA1 and CA3, and the primary and secondary visual cortices. Our results demonstrate that RP and RQA are able to reveal the alterations in the brain caused by AD and aging.

We acknowledge that our approach in revealing the effects of AD on brain function is comparative, meaning that the detection of AD using this method requires comparison to a control group. However, we state that this work, functions as a proof of concept, that RQA can in fact capture the intrinsic patterns of neural activity recorded by rs-fMRI images discriminatively and with high confidence as proven by our statistical tests. Furthermore, while the high dimensionality of the RP and RQA method is a substantial part of their benefits, it increases the computational complexities of the approach significantly. In the future, we suggest studies with clinical research on humans or animals with larger number of samples is conducted to (a) advance the knowledge into the alterations of the brain as the result of early-stage AD and assess the abilities of RQA in describing rs-fMRI data more deeply, and (b) combine RQA with other diagnostic tools such as machine learning and deep learning techniques to improve early detection of AD. Additional studies into reducing the computational cost of RQA while keeping the benefits may be advantageous. In addition, further research can be conducted to translate the findings of this study to humans and follow-up on how these patterns of neural alterations can assist the diagnosis of AD at early stages.

## Code availability

The codes related to this study are available at <https://github.com/>

## Appendix 1

**Table A1**

Summarizes the DMLN regions, including each region's identifier, structure name, and abbreviation based on the Fischer344 atlas.

| Structure    | Cingulate Cortex<br>Area 1 | Cingulate Cortex<br>Area 2 | Orbitofrontal<br>Cortex | Prelimbic<br>Cortex      | Infralimbic<br>Cortex    | Primary Visual<br>Cortex | Parietal Association<br>Cortex |
|--------------|----------------------------|----------------------------|-------------------------|--------------------------|--------------------------|--------------------------|--------------------------------|
| Abbreviation | CG1                        | CG2                        | OFC                     | PrL                      | IL                       | V1                       | PtA                            |
| Structure    | Retrosplenial<br>Cortex    | Secondary Visual<br>Cortex | Temporal<br>Association | Hippocampal Field<br>CA1 | Hippocampal Field<br>CA2 | Hippocampal Field<br>CA3 | Basal<br>forebrain             |
| Abbreviation | RSC                        | V2                         | TeA                     | CA1                      | CA2                      | CA3                      | BFB                            |

Research-lab-KUMS/AD\_RQA. The pre-processing steps for fMRI data utilized the open-source SPM12 software (Statistical Parametric Mapping) and the Advanced Normalization Tools (ANTS). Following this, we applied recurrence quantification analysis of the data, using the Cross Recurrence Plot (CRP) Toolbox in MATLAB. The statistical analysis and visualizations were performed in Python.

## CRediT authorship contribution statement

**Arash Rezaei:** Conceptualization, Formal analysis, Software, Writing – original draft. **Monica van den Berg:** Investigation, Methodology, Software, Writing – review & editing. **Hajar Mirlohi:** Methodology, Writing – review & editing. **Marleen Verhoye:** Conceptualization, Writing – review & editing. **Mahmood Amiri:** Conceptualization, Supervision, Writing – review & editing. **Georgios A. Keliris:** Supervision, Writing – review & editing.

## Declaration of competing interest

The authors declare that they have no known competing financial interests or personal relationships that could have appeared to influence the work reported in this paper.

## Acknowledgments

The authors would like to thank the esteemed reviewers for their insightful and helpful comments. This study was supported by the Scientific Research Flanders (FWO- G048917N, FWO-G045420N), the Stichting Alzheimer Onderzoek (SAO-FRA-20180003), the European Union's Horizon 2020 research and innovation program under the Marie Skłodowska-Curie grant agreement No 101007926 and the Hellenic Foundation Research Institute (HFRI) under the project neuron-AD (project number 04058).

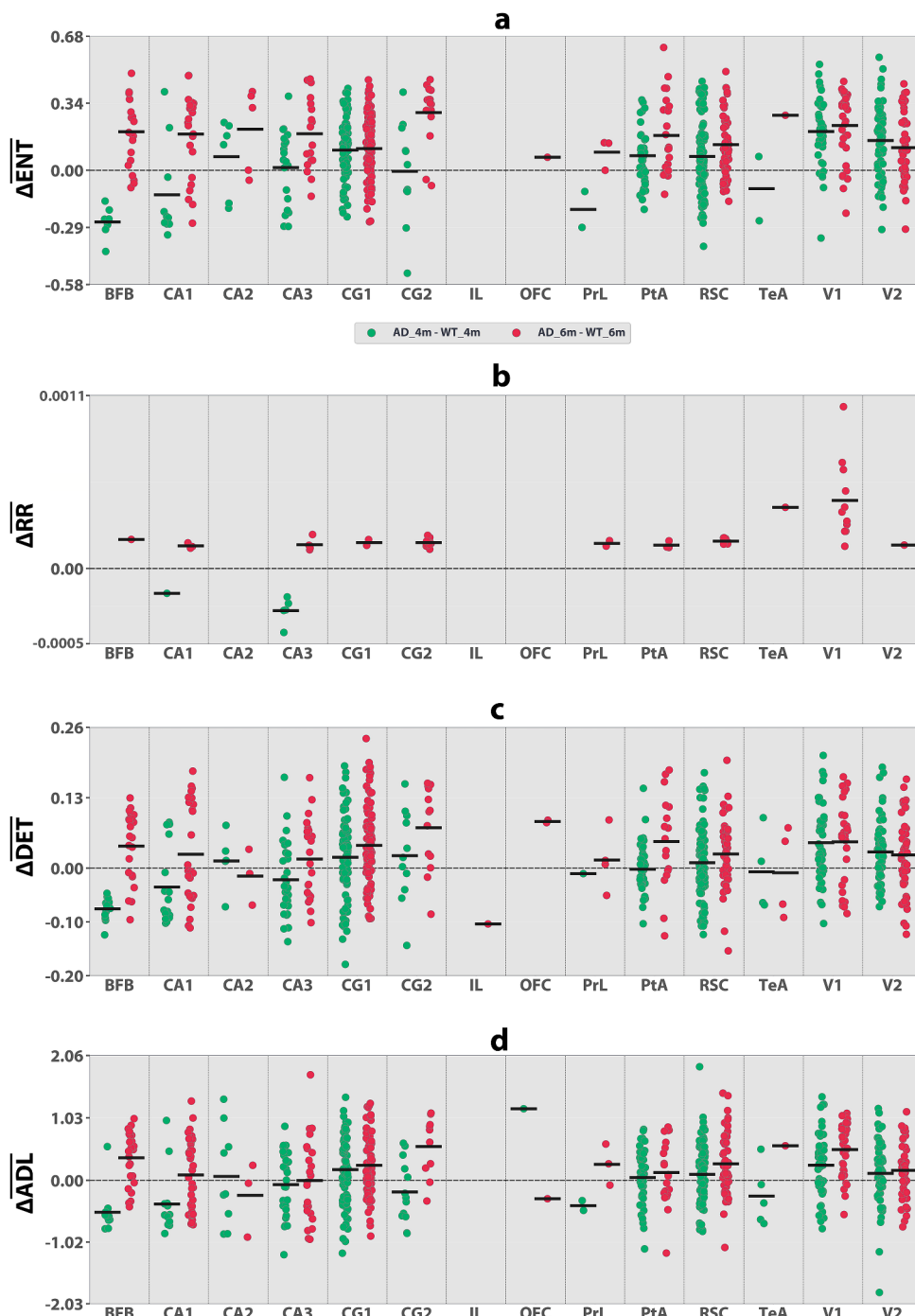


**Fig. A1.** Results of the comparison between AD and WT rats using the RQA method in the DMLN regions with  $\epsilon = 4.58$  (5 % of mean PSD). Green\Red circles represents comparison of 4m\6 m groups and the black lines indicates the mean value of the features in a specific region. a) The differences of ENT in AD\_4m - WT\_4m and AD\_6m - WT\_6m. b) The differences of RR in AD\_4m - WT\_4m and AD\_6m - WT\_6m. c) The differences of DET in AD\_4m - WT\_4m and AD\_6m - WT\_6m. d) The differences of ADL in AD\_4m - WT\_4m and AD\_6m - WT\_6m. BFB: basal forebrain, CA1: hippocampal field 1, CA2: hippocampal field 2, CA3: hippocampal field 3, CG1: cingulate cortex area 1, CG2: cingulate cortex area 2, IL: infralimbic cortex, OFC: orbitofrontal cortex, PrL: prelimbic cortex, PtA: parietal association cortex, RSC: retrosplenial cortex, TeA: temporal association cortex, V1: primary visual cortex, V2: secondary visual cortex.

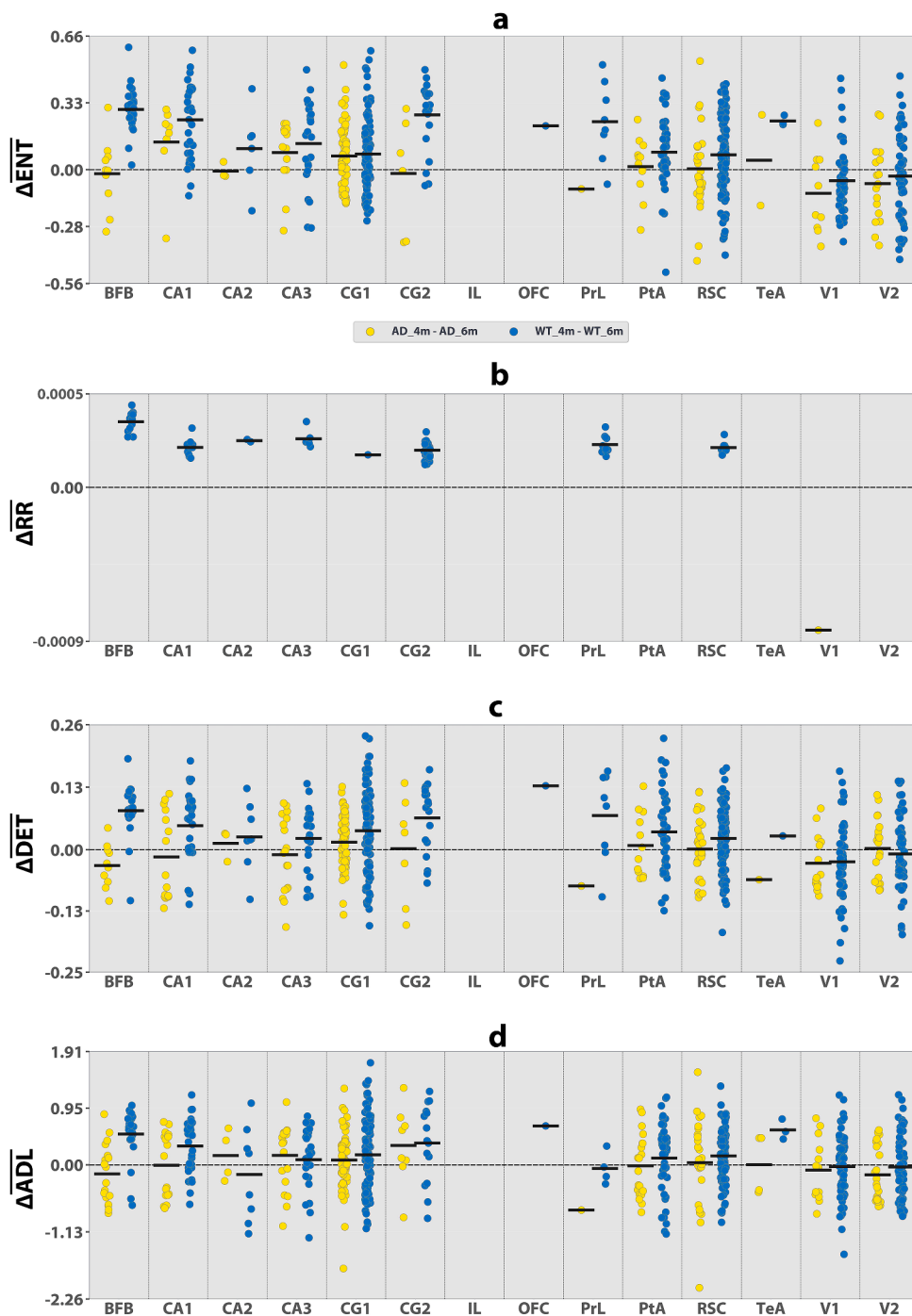


**Fig. A2.** Results of the comparison between 4-and 6-months rats using the RQA method in the DMLN regions with  $\epsilon = 4.58$  (5 % of mean PSD). Yellow\Blue circles represents comparison of AD\WT groups and the black lines indicates the mean value of the features in a specific region. a) The differences of ENT in AD\_4m – AD\_6m and WT\_4m – WT\_6m. b) The differences of RR in AD\_4m – AD\_6m and WT\_4m – WT\_6m. c) The differences of DET in AD\_4m – AD\_6m and WT\_4m – WT\_6m. d) The differences of ADL in AD\_4m – AD\_6m and WT\_4m – WT\_6m. BFB: basal forebrain, CA1: hippocampal field 1, CA2: hippocampal field 2, CA3: hippocampal field 3, CG1: cingulate cortex area 1, CG2: cingulate cortex area 2, IL: infralimbic cortex, OFC: orbitofrontal cortex, PrL: prelimbic cortex, PtA: parietal association cortex, RSC: retrosplenial cortex, TeA: temporal association cortex, V1: primary visual cortex, V2: secondary visual cortex.

## References

- [1] GDF, Collaborators, Estimation of the global prevalence of dementia in 2019 and forecasted prevalence in 2050: an analysis for the Global Burden of Disease Study 2019," (in eng), Lancet Public Health 7 (2) (2022) e105–e125, [https://doi.org/10.1016/s2468-2667\(21\)00249-8](https://doi.org/10.1016/s2468-2667(21)00249-8).
- [2] D.W. Dickson, The pathogenesis of senile plaques," (in eng), J. Neuropathol. Exp. Neurol. 56 (4) (1997) 321–339, <https://doi.org/10.1097/00005072-199704000-00001>.
- [3] J.L. Crimins, A. Pooler, M. Polydoro, J.I. Luebke, T.L. Spires-Jones, The intersection of amyloid  $\beta$  and tau in glutamatergic synaptic dysfunction and collapse in Alzheimer's disease (in eng), Ageing Res. Rev. 12 (3) (2013) 757–763, <https://doi.org/10.1016/j.arr.2013.03.002>.
- [4] Anon. A. s. Association. "2021 Alzheimer's disease facts and figures." <https://www.alz.org/alzheimers-dementia/facts-figures> (accessed 2022).
- [5] R.J. Perrin, A.M. Fagan, D.M. Holtzman, Multimodal techniques for diagnosis and prognosis of Alzheimer's disease, Nature 461 (7266) (2009) 916–922, <https://doi.org/10.1038/nature08538>, 2009/10/01.

- [6] S.W. Scheff, D.A. Price, F.A. Schmitt, E.J. Mufson, Hippocampal synaptic loss in early Alzheimer's disease and mild cognitive impairment, *Neurobiol. Aging* 27 (10) (2006) 1372–1384, <https://doi.org/10.1016/j.neurobiolaging.2005.09.012>, 2006/10/01/.
- [7] C.H. Andrade-Moraes, et al., Cell number changes in Alzheimer's disease relate to dementia, not to plaques and tangles (in eng), *Brain* 136 (2013) 3738–3752, <https://doi.org/10.1093/brain/awt273>. no. Pt 12.
- [8] S.E. Counts, M.D. Ikonomovic, N. Mercado, I.E. Vega, E.J. Mufson, Biomarkers for the early detection and progression of Alzheimer's disease (in eng), *Neurotherapeutics* 14 (1) (2017) 35–53, <https://doi.org/10.1007/s13311-016-0481-z>.
- [9] E. Bayram, J.Z.K. Caldwell, S.J. Banks, Current understanding of magnetic resonance imaging biomarkers and memory in Alzheimer's disease (in eng), *Alzheimers. Dement.* 4 (2018) 395–413, <https://doi.org/10.1016/j.jrci.2018.04.007> (N. Y).
- [10] N.K. Logothetis, The neural basis of the blood-oxygen-level-dependent functional magnetic resonance imaging signal (in eng), *Philos. Trans. R. Soc. Lond. B Biol. Sci.* 357 (1424) (2002) 1003–1037, <https://doi.org/10.1098/rstb.2002.1114>.
- [11] M. Odusami, R. Maskeliūnas, R. Damasevičius, T. Krilavičius, Analysis of features of Alzheimer's disease: detection of early stage from functional brain changes in magnetic resonance images using a finetuned ResNet18 network (in eng), *Diagnostics* 11 (6) (2021), <https://doi.org/10.3390/diagnostics11061071>. (Basel) Jun 10.
- [12] H. Padole, S.D. Joshi, T.K. Gandhi, Early detection of Alzheimer's disease using graph signal processing on neuroimaging data, in: Proceedings of the 2018 2nd European Conference on Electrical Engineering and Computer Science (EECS), 2018, pp. 302–306, <https://doi.org/10.1109/EECS.2018.00062>, 20–22 Dec. 2018.
- [13] R. Ju, C. Hu, z. p. Q. Li, Early diagnosis of Alzheimer's disease based on resting-state brain networks and deep learning, *IEEE ACM Trans. Comput. Biol. Bioinform.* 16 (1) (2019) 244–257, <https://doi.org/10.1109/TCBB.2017.2776910>.
- [14] M.N.I. Qureshi, S. Ryu, J. Song, K.H. Lee, B. Lee, Evaluation of functional decline in Alzheimer's dementia using 3D deep learning and group ICA for rs-fMRI measurements (in English), *Front. Aging Neurosci.* 11 (2019), <https://doi.org/10.3389/fnagi.2019.00008>. Original Research2019–February–11.
- [15] A. Alorff, M.U.G. Khan, Multi-label classification of Alzheimer's disease stages from resting-state fMRI-based correlation connectivity data and deep learning, *Comput. Biol. Med.* 151 (2022) 106240, <https://doi.org/10.1016/j.combiomed.2022.106240>, 2022/12/01/.
- [16] J. Liu, G. Tan, W. Lan, J. Wang, Identification of early mild cognitive impairment using multi-modal data and graph convolutional networks, *BMC Bioinform.* 21 (6) (2020) 123, <https://doi.org/10.1186/s12859-020-3437-6>, 2020/11/18.
- [17] B. Lei, et al., Multi-scale enhanced graph convolutional network for mild cognitive impairment detection, *Pattern. Recognit.* 134 (2023) 109106, <https://doi.org/10.1016/j.patcog.2022.109106>, 2023/02/01/.
- [18] X. Tian, Y. Liu, L. Wang, X. Zeng, Y. Huang, Z. Wang, An extensible hierarchical graph convolutional network for early Alzheimer's disease identification, *Comput. Methods Programs Biomed.* 238 (2023) 107597, <https://doi.org/10.1016/j.cmpb.2023.107597>, 2023/08/01/.
- [19] Y. Kazemi, S. Houghten, A deep learning pipeline to classify different stages of Alzheimer's disease from fMRI data, in: Proceedings of the 2018 IEEE Conference on Computational Intelligence in Bioinformatics and Computational Biology (CIBCB), 2018, pp. 1–8, <https://doi.org/10.1109/CIBCB.2018.8404980>, 30 May–2 June 2018.
- [20] T. Tajammal, S.K. Khurshid, A. Jaleel, S.Q. Wahla, R.A. Ziar, Deep learning-based ensembling technique to classify alzheimer's disease stages using functional MRI (in eng), *J. Healthc. Eng.* (2023) 6961346, <https://doi.org/10.1155/2023/6961346>. vol. 2023.
- [21] A.A. Mukhlif, B. Al-Khateeb, M.A. Mohammed, An extensive review of state-of-the-art transfer learning techniques used in medical imaging: open issues and challenges, *J. Intell. Syst.* 31 (1) (2022) 1085–1111, <https://doi.org/10.1515/jisy-2022-0198>.
- [22] X. Liu, N. Zhang, C. Chang, J.H. Duyn, Co-activation patterns in resting-state fMRI signals (in eng), *Neuroimage* 180 (2018) 485–494, <https://doi.org/10.1016/j.neuroimage.2018.01.041>. no. Pt B.
- [23] F. He, Y. Yang, Nonlinear system identification of neural systems from neurophysiological signals (in eng), *Neuroscience* 458 (2021) 213–228, <https://doi.org/10.1016/j.neuroscience.2020.12.001>.
- [24] A. Lundervold, On consciousness, resting state fMRI, and neurodynamics (in eng), *Nonlinear Biomed. Phys.* 4 (1) (2010) S9, <https://doi.org/10.1186/1753-4631-4-s1-s9>. Suppl 1, no. Suppl.
- [25] A. Lombardi, P. Guccione, L. Mascolo, Analysis of fMRI data using the complex systems approach, in: Proceedings of the 20th IMEKO TC-4 International Symposium on Measurements of Electrical Quantities, Benevento, 2014, pp. 15–17.
- [26] J.P. Eckmann, S.O. Kamphorst, D. Ruelle, Recurrence plots of dynamical systems, *Europhys. Lett.* 4 (9) (1987) 973, <https://doi.org/10.1209/0295-5075/4/9/004>, 1987/11/01.
- [27] C. Webber, N. Marwan, Recurrence Quantification Analysis – Theory and Best Practices (Understanding Complex Systems), Springer, Cham, 2015, p. 421.
- [28] M. Amiri, E. Davoodi-Bojd, F. Bahrami, M. Raza, Bifurcation analysis of the Poincaré map function of intracranial EEG signals in temporal lobe epilepsy patients, *Math. Comput. Simul.* 81 (11) (2011) 2471–2491, <https://doi.org/10.1016/j.matcom.2011.03.012>, 2011/07/01/.
- [29] G. Orlando, G. Zimatore, Recurrence quantification analysis of business cycles, *Chaos Solit. Fractals* 110 (2018) 82–94, <https://doi.org/10.1016/j.chaos.2018.02.032>, 2018/05/01/.
- [30] Q. Wu, M. Wang, L. Tian, The market-linkage of the volatility spillover between traditional energy price and carbon price on the realization of carbon value of emission reduction behavior, *J. Clean. Prod.* 245 (2020) 118682, <https://doi.org/10.1016/j.jclepro.2019.118682>, 2020/02/01/.
- [31] L. Billeci, D. Marino, L. Insana, G. Vatti, M. Varanini, Patient-specific seizure prediction based on heart rate variability and recurrence quantification analysis, *PLoS One* 13 (9) (2018) e0204339, <https://doi.org/10.1371/journal.pone.0204339>.
- [32] O. Afsar, U. Tirnakli, N. Marwan, Recurrence quantification analysis at work: quasi-periodicity based interpretation of gait force profiles for patients with Parkinson disease, *Sci. Rep.* 8 (1) (2018) 9102, <https://doi.org/10.1038/s41598-018-27369-2>, 2018/06/14.
- [33] X. Gao, X. Yan, P. Gao, X. Gao, S. Zhang, Automatic detection of epileptic seizure based on approximate entropy, recurrence quantification analysis and convolutional neural networks, *Artif. Intell. Med.* 102 (2020) 101711, <https://doi.org/10.1016/j.artmed.2019.101711>, 2020/01/01/.
- [34] X. Meng, S. Qiu, S. Wan, K. Cheng, L. Cui, A motor imagery EEG signal classification algorithm based on recurrence plot convolution neural network, *Pattern. Recognit. Lett.* 146 (2021) 134–141, <https://doi.org/10.1016/j.patrec.2021.03.023>, 2021/06/01/.
- [35] G. Baghdadi, M. Amiri, E. Falotico, C. Laschi, Recurrence quantification analysis of EEG signals for tactile roughness discrimination, *Int. J. Mach. Learn. Cybern.* 12 (4) (2021) 1115–1136, <https://doi.org/10.1007/s13042-020-01224-1>, 2021/04/01.
- [36] A.L. Moraes, R.A.S. Fernandes, Recurrence plots: a novel feature engineering technique to analyze power quality disturbances, in: Proceedings of the 2020 IEEE Power & Energy Society General Meeting (PESGM), 2020, pp. 1–5, <https://doi.org/10.1109/PESGM41954.2020.9281699>, 2–6 Aug. 2020.
- [37] K. Ciecielak, K. Kecik, K. Zaleski, Defects detection from time series of cutting force in composite milling process by recurrence analysis, *J. Reinf. Plast. Compos.* 39 (23–24) (2020) 890–901, <https://doi.org/10.1177/0731684420935985>.
- [38] C. Rodriguez-Sabate, M. Rodriguez, I. Morales, Studying the functional connectivity of the primary motor cortex with the binarized cross recurrence plot: the influence of Parkinson's disease, *PLoS One* 16 (6) (2021) e0252565, <https://doi.org/10.1371/journal.pone.0252565>.
- [39] P. Anastasia, et al., Altered hippocampal connectivity dynamics predicts memory performance in neuropsychiatric lupus: a resting-state fMRI study using cross-recurrence quantification analysis, *Lupus. Sci. Med.* 10 (2) (2023) e000920, <https://doi.org/10.1136/lupus-2023-000920>.
- [40] K. Borkar, A. Chaturvedi, P.K. Vinod, R.S. Bapi, Ayu-characterization of healthy aging from neuroimaging data with deep learning and rsfMRI (in English), *Front. Comput. Neurosci.* 16 (2022), <https://doi.org/10.3389/fncom.2022.940922>. Original Research2022–September–12.
- [41] F. Xu, et al., An explainable autoencoder with multi-paradigm fMRI fusion for identifying differences in dynamic functional connectivity during brain development, *Neural Netw.* 159 (2023) 185–197, <https://doi.org/10.1016/j.neunet.2022.12.007>, 2023/02/01/.
- [42] H. Ahmadi, E. Fatemizadeh, A. Motie-Nasrabadi, Deep sparse graph functional connectivity analysis in AD patients using fMRI data, *Comput. Methods Programs Biomed.* 201 (2021) 105954, <https://doi.org/10.1016/j.cmpb.2021.105954>, 2021/04/01/.
- [43] W. Majeed, M. Magnuson, S.D. Keilholz, Spatiotemporal dynamics of low frequency fluctuations in BOLD fMRI of the rat, *J. Magn. Reson. Imaging* 30 (2) (2009) 384–393, <https://doi.org/10.1002/jmri.21848>.
- [44] M.E. Beloy, et al., Quasi-periodic patterns of neural activity improve classification of Alzheimer's disease in mice, *Sci. Rep.* 8 (1) (2018) 10024, <https://doi.org/10.1038/s41598-018-28237-9>, 2018/07/03.
- [45] R.M. Cohen, et al., A transgenic Alzheimer rat with plaques, tau pathology, behavioral impairment, oligomeric  $\alpha$  $\beta$ , and frank neuronal loss (in eng), *J. Neurosci.* 33 (15) (2013) 6245–6256, <https://doi.org/10.1523/jneurosci.3672-12.2013>.
- [46] I.L. Joo, et al., Early neurovascular dysfunction in a transgenic rat model of Alzheimer's disease, *Sci. Rep.* 7 (1) (2017) 46427, <https://doi.org/10.1038/srep46427>, 2017/04/12.
- [47] H. Braak, D.R. Thal, E. Ghebremedhin, K. Del Tredici, Stages of the pathologic process in Alzheimer disease: age categories from 1 to 100 years (in eng), *J. Neuropathol. Exp. Neurol.* 70 (11) (2011) 960–969, <https://doi.org/10.1097/NEN.0b013e318232a379>.
- [48] M. van den Berg, et al., Altered basal forebrain function during whole-brain network activity at pre- and early-plaque stages of Alzheimer's disease in TgF344-AD rats (in eng), *Alzheimers Res. Ther.* 14 (1) (2022) 148, <https://doi.org/10.1186/s13195-022-01089-2>. Oct 10.
- [49] D. Goerzen, et al., An MRI-derived neuroanatomical atlas of the Fischer 344 rat brain, *Sci. Rep.* 10 (1) (2020) 6952, <https://doi.org/10.1038/s41598-020-63965-x>, 2020/04/24.
- [50] L.M. Peeters, M. van den Berg, R. Hinz, G. Majumdar, I. Pintelon, G.A. Keliris, Cholinergic modulation of the default mode like network in rats, *iScience* 23 (9) (2020) 101455, <https://doi.org/10.1016/j.isci.2020.101455>, 2020/09/25/.
- [51] N. Takata, N. Sato, Y. Komaki, H. Okano, K.F. Tanaka, Flexible annotation atlas of the mouse brain: combining and dividing brain structures of the Allen Brain Atlas while maintaining anatomical hierarchy, *Sci. Rep.* 11 (1) (2021) 6234, <https://doi.org/10.1038/s41598-021-85807-0>, 2021/03/18.
- [52] Anon. Allen institute for brain science. Allen mouse brain atlas.2024 [Online]. Available: [mouse.brain-map.org](http://mouse.brain-map.org).
- [53] E. Yargholi, A.M. Nasrabadi, Recurrence quantification analysis of electroencephalogram signals during standard tasks of Waterloo-Stanford group

- scale of hypnotic susceptibility, *J. Med. Eng. Technol.* 39 (1) (2015) 26–34, <https://doi.org/10.3109/03091902.2014.973616>, 2015/01/02.
- [54] F. Takens, D. Rand, L.S. Young, Detecting strange attractors in turbulence. *Dynamical Systems and Turbulence*, Warwick, Springer Berlin Heidelberg, Berlin, Heidelberg, 1980, pp. 366–381. Eds., 1981//1981.
- [55] J. Zbilut, C. Webber, Embeddings and delays as derived from quantification of recurrence plots, *Phys. Lett. A* 171 (1992) 199–203, [https://doi.org/10.1016/0375-9601\(92\)90426-M](https://doi.org/10.1016/0375-9601(92)90426-M), 12/01.
- [56] N. Marwan, M. Carmen Romano, M. Thiel, J. Kurths, Recurrence plots for the analysis of complex systems, *Phys. Rep.* 438 (5) (2007) 237–329, <https://doi.org/10.1016/j.physrep.2006.11.001>, 2007/01/01.
- [57] S. Wallot, D. Mönster, Calculation of average mutual information (AMI) and false-nearest neighbors (FNN) for the estimation of embedding parameters of multidimensional time series in matlab (in English),, *Front. Psychol.* 9 (2018), <https://doi.org/10.3389/fpsyg.2018.01679>. Technology Report2018-September-10.
- [58] A.M. Fraser, H.L. Swinney, Independent coordinates for strange attractors from mutual information, *Phys. Rev. A* 33 (2) (1986) 1134–1140, <https://doi.org/10.1103/PhysRevA.33.1134>, 02/01/.
- [59] C. Webber, J. Zbilut, Recurrence quantification analysis of nonlinear dynamical systems, *Tutor. Contemp. Nonlinear Methods Behav. Sci.* (2005), 01/01.
- [60] A. Lombardi, P. Guccione, L. Mascolo, P. Taurisano, L. Fazio, G. Nico, Combining graph analysis and recurrence plot on fMRI data, in: Proceedings of the 2015 IEEE International Symposium on Medical Measurements and Applications (MeMeA), 2015, pp. 18–23, <https://doi.org/10.1109/MeMeA.2015.7145165>, 7-9 May 2015.
- [61] M.B. Kennel, R. Brown, H.D. Abarbanel, Determining embedding dimension for phase-space reconstruction using a geometrical construction (in eng), *Phys. Rev. A* 45 (6) (1992) 3403–3411, <https://doi.org/10.1103/physreva.45.3403>.
- [62] L. Cao, Practical method for determining the minimum embedding dimension of a scalar time series, *Phys. D Nonlinear Phenom.* 110 (1) (1997) 43–50, [https://doi.org/10.1016/S0167-2789\(97\)00118-8](https://doi.org/10.1016/S0167-2789(97)00118-8), 1997/12/01.
- [63] K. Bielski, S. Adamus, E. Kolada, J. Račzaszek – Leonardi, I. Szatkowska, Parcellation of the human amygdala using recurrence quantification analysis, *Neuroimage* 227 (2021) 117644, <https://doi.org/10.1016/j.neuroimage.2020.117644>, 2021/02/15/.
- [64] D. Makowski, et al., NeuroKit2: a Python toolbox for neurophysiological signal processing, *Behav. Res. Methods* 53 (4) (2021) 1689–1696, <https://doi.org/10.3758/s13428-020-01516-y>, 2021/08/01.
- [65] S. Schinkel, O. Dimigen, N. Marwan, Selection of recurrence threshold for signal detection, *Eur. Phys. J. Spec. Top.* 164 (2008) 15–53, <https://doi.org/10.1140/epjst/e2008-00833-5>, 10/01.
- [66] Anon. Cross Recurrence Plot Toolbox for MATLAB®, Ver. 5.22 (R33.2).2024 Accessed: 2021-10-28. [Online]. Available: [http://tocsy.pik-potsdam.de/CRPttoolbox/](http://tocsy.pik-potsdam.de/CRPtoolbox/).
- [67] J. Zbilut, C. Webber, Recurrence quantification analysis: introduction and historical context," *I. J. Bifurcation Chaos* 17 (2007) 3477–3481, <https://doi.org/10.1142/S0218127407019238>, 10/01.
- [68] S.V. Ovsepian, V.B. O’Leary, C. Hoschl, L. Zaborszky, Integrated phylogeny of the human brain and pathobiology of Alzheimer’s disease: a unifying hypothesis, *Neurosci. Lett.* 755 (2021) 135895, <https://doi.org/10.1016/j.neulet.2021.135895>, 2021/06/1/.
- [69] X. Liu, et al., Effects of APOE e2 allele on basal forebrain functional connectivity in mild cognitive impairment (in eng), *CNS Neurosci. Ther.* 29 (2) (2023) 597–608, <https://doi.org/10.1111/cns.14038>.
- [70] P.A. Chiesa, et al., Relationship between basal forebrain resting-state functional connectivity and brain amyloid- $\beta$  deposition in cognitively intact older adults with subjective memory complaints (in eng),, *Radiology* 290 (1) (2019) 167–176, <https://doi.org/10.1148/radiol.2018180268>.
- [71] S. De Waegenaere, M. van den Berg, G.A. Keliris, M.H. Adhikari, M. Verhoye, Early altered directionality of resting brain network state transitions in the TgF344-AD rat model of Alzheimer’s disease (in English),, *Front. Hum. Neurosci.* 18 (2024), <https://doi.org/10.3389/fnhum.2024.1379923>. Original Research2024-April-05.
- [72] O.A. Shipton, C.S. Tang, O. Paulsen, M. Vargas-Caballero, Differential vulnerability of hippocampal CA3-CA1 synapses to A $\beta$ , *Acta Neuropathol. Commun.* 10 (1) (2022) 45, <https://doi.org/10.1186/s40478-022-01350-7>, 2022/04/04.
- [73] A. Papanikolaou, F.R. Rodrigues, J. Holeniewska, K.G. Phillips, A.B. Saleem, S. G. Solomon, Plasticity in visual cortex is disrupted in a mouse model of tauopathy, *Commun. Biol.* 5 (1) (2022) 77, <https://doi.org/10.1038/s42003-022-03012-9>, 2022/01/20.
- [74] Z. Wang, Brain entropy mapping in healthy aging and Alzheimer’s disease (in eng),, *Front. Aging Neurosci.* 12 (2020) 596122, <https://doi.org/10.3389/fnagi.2020.596122>.